GPS Solutions (2025) 29:26
https://doi.org/10.1007/s10291-024-01779-4

ORIGINAL ARTICLE

Ionospheric tomography for SWARM satellite orbit determination using single-frequency GNSS data

Fabricio S. Prol[1,2] · Alessio Pignalberi[3] · Artem Smirnov[4,5] · Michael Pezzopane[3] · Ana L. Christovam[6] · Kannan Selvan[2] · Mainul Hoque[7] · Sanna Kaasalainen[1]

Received: 10 June 2024 / Accepted: 8 November 2024 / Published online: 25 November 2024

Abstract
Ionospheric tomography offers three-dimensional (3D) description of the electron density distribution, enabling the direct incorporation of electron density data into the slant total electron content (STEC) computation. As a result, STEC derived from tomography helps mitigate the ionospheric delay experienced in the line of sight between global navigation satellite systems (GNSS) and satellites positioned in low Earth orbits (LEO). Tomography can therefore be effectively employed to correct single-frequency GNSS observations and allow enhanced positioning of spaceborne platforms. We demonstrate the accuracy and performance of a global-scale ionospheric tomography method for determining satellite orbits, utilizing single-frequency GNSS measurements combined with a precise point positioning (PPP) algorithm. We compare the tomographic outcomes against orbit determination derived from the GRoup and PHase ionospheric correction (GRAPHIC) observable and based on an ionospheric climatological model. Near the peak of solar cycle 24, the overall accuracy achieved with tomography was around 3.8 m. notably, compared to the background climatological model, tomography demonstrated improvements ranging from 15 to 20%. The GRAPHIC method outperformed tomography, achieving an accuracy of 0.7 m, whereas we obtained around 7 m accuracy when no ionospheric model is employed. Although the developed ionospheric tomography has yet to match the precision of GRAPHIC, our results bring us relatively closer to this objective.

Keywords Low earth orbit · Ionosphere · Swarm · GPS · Tomography · GRAPHIC · Geomagnetic storm

Introduction

Among the empirical techniques to describe the ionosphere (Forootan et al. 2023; Aa et al. 2023; Tsagouri et al. 2023), ionospheric tomography stands out as one of the most accurate (Wang et al. 2023). Ionospheric tomography provide accurate observations of the ionospheric electron density over regional areas (Wen et al. 2022; Norberg et al. 2023; Long et al. 2023; Zheng et al. 2023), capturing medium-to-small-scale phenomena such as traveling ionospheric disturbances (Chen et al. 2024), geomagnetic storm signatures in polar regions (Pokhotelov et al. 2021; Shan et al. 2022), solar eclipses (Chen et al. 2022), and earthquake-induced disturbances (Zhai et al. 2021). Tomography has also been employed to enhance global navigation satellite systems (GNSS) augmentation systems (Yin et al. 2022) and precise point positioning (PPP) techniques (Prol et al. 2024). More recently, global-scale solutions have emerged (Mei et al. 2023), expanding the applications of tomography

✉ Fabricio S. Prol
fabricio.dossantosprol@nls.fi

1 Department of Navigation and Positioning, Finnish Geospatial Research Institute (FGI), Espoo 02150, Finland

2 School of Technology and Innovations, University of Vaasa, Wolffintie 32, Vaasa 65200, Finland

3 Istituto Nazionale di Geofisica e Vulcanologia (INGV), Via di Vigna Murata 605, 00143 Roma, Italy

4 Department of Earth and Environmental Sciences, Ludwig Maximilian University of Munich (LMU), Theresienstraße 41, 80333 Munich, Germany

5 Helmholtz Centre Potsdam, GFZ German Research Centre for Geosciences, 14473 Telegrafenberg, Potsdam, Germany

6 Department of Cartography, São Paulo State University (UNESP), Presidente Prudente, São Paulo 19060-900, Brazil

7 Institute for Solar-Terrestrial Physics, German Aerospace Center (DLR), Kalkhorstweg 53, 17235 Neustrelitz, Germany

to describe the three-dimensional (3D) ionosphere over sparsely covered regions.

Global tomography can be used for satellite orbit determination with single-frequency GNSS receivers. As this capability is not achievable with regional solutions, it is particularly appealing to the space industry. Satellite orbit determination with single-frequency GNSS receivers is essential for several satellites in low Earth orbits (LEO). Müller et al. (2024), for instance, developed specific algorithms for the Astrocast satellite constellation based on single-frequency GNSS receivers. Kovář (2017) built a single-frequency receiver specifically designed for small satellite missions. Conrad et al. (2023) presented distinct strategies adopted for orbit determination with single-frequency receivers onboard the LEO satellites of the CYGNSS mission. These studies are relevant since single-frequency GNSS receivers help the satellite mission to meet the basic navigation requirements (Garcia-Fernàndez et al., 2006). This energy-saving attribute occurs because these receivers consume $30-40\%$ less energy compared to their dual-frequency counterparts (Karki 2020), allowing substantial optimization of the spacecraft mass and overall mission cost. Optimizing satellite efficiency is particularly important in the upcoming years, as the modernization of miniaturized components has brought up an increased number of small satellites, which are even constituting mega-constellations.

Earlier works evaluated ionospheric models and GNSS linear combinations for the task of satellite orbit determination with single-frequency receivers. Montenbruck (2003) showed a method for kinematic point positioning where the ionospheric delay is corrected using the GRoup and PHase Ionospheric Correction (GRAPHIC) combination. They obtained 3D accuracies at a level of 1–1.5 m. Montenbruck and González Rodríguez (2020) evaluated the NeQuick-G performance for satellite orbit determination, achieving an accuracy of around 2–5 m (1-sigma), depending on the solar cycle. Bock et al. (2009) showed three different approaches for orbit determination with single frequency data: (1) based on global ionospheric maps (GIMs); (2) GRAPHIC linear combination; and (3) estimating the ionospheric delay as a parameter in the least squares adjustment. They showed that the satellite orbit determination using GRAPHIC method achieves decimeter level accuracy whereas the other methods were accurate at the metric level. Dong-Ju and Bin (2012) applied GIMs using an ionospheric scale factor in kinematic and dynamic orbit determination with single-frequency measurements. The authors showed 3D accuracies at a level of about 2 m.

Common to previous works is the fact that GRAPHIC observables provide better results in comparison to ionospheric models. Nevertheless, the conducted evaluations are essential for identifying the limitations of the ionospheric models, which in turn guide recommendations for further enhancements. Additionally, even though ionospheric models have not been better than GRAPHIC solutions, they still play a crucial role in mitigating high-order effects on the ionosphere, which is essential even with the dual-frequency GNSS receivers (Qi et al. 2021; Guo et al. 2023). In continuation of the existing research, we extend the comparison of the GRAPHIC observable versus ionospheric models by evaluating the accuracy of the global-scale ionospheric tomography previously developed by Prol et al. (2021a). Three ionospheric/plasmaspheric models were chosen for the analysis. The Neustrelitz electron density model (NEDM) (Hoque et al. 2022) serves as a reference for a climatological model. The tomographic approach developed by Prol et al. (2021a) offers a high-resolution 3D representation of the ionosphere and plasmasphere. Additionally, a daily ionospheric model is developed to assess the performance of two-dimensional (2D) representations of vertical total electron content (VTEC) using a single Swarm satellite. Our primary objective is to demonstrate the feasibility of employing tomography for satellite orbit determination, providing an expected accuracy of these solutions in comparison to other models. The next section presents the case study, datasets, and methods. The achieved accuracy is shown in the Results section. Conclusions are outlined in the last section.

Materials and methods

Case study and dataset

To perform our investigation, we have selected the week of March 14th to 20th, 2015, as our case study. This time frame was chosen because the tomography technique being studied has been comprehensively evaluated during these periods. We utilize the exact same tomographic results obtained by Prol et al. (2021a) as input for satellite orbit determination. This ensures that the tomographic solutions evaluated here maintain accurate representations of the peak height of the ionosphere and the topside region, as validated against ionosonde and in-situ observations. While we have previously observed that the global-scale tomography can effectively capture signatures of the impact of the St. Patrick's Day geomagnetic storm on the ionosphere, it remains uncertain how such a high-resolution 3D ionospheric model would perform for satellite orbit determination.

The period under consideration includes the 2015 St. Patrick geomagnetic storm, the most intense observed during the 24th solar cycle. The storm was prompted by a coronal mass ejection that hit the Earth magnetosphere on 17 March causing the sudden storm commencement at around

04:45 Universal Time (UT), while the maximum intensity was reached at around 23:00 UT of 17 March (Kamide and Kusano 2015). The main phase of the storm was followed by a long recovery phase lasting several days, which included severe sub-storm activity at high latitudes. It was classified as a severe geomagnetic storm characterized by a minimum value of the D_{st} index of -223 nT, while the K_p index reached a maximum value of 8. During the main phase of the storm, two electron density peaks were detected at magnetic latitudes higher than 30° N and 30° S in the Atlantic Ocean region (Pignalberi et al. 2016), suggesting the presence of a "super-fountain effect" (e.g., Balan et al. 2010).

To test the satellite orbit determination, we utilize GNSS data collected by the Swarm-A satellite. Swarm-A is one of the three LEO satellites composing the ESA's Swarm constellation launched at the end of 2013 and still operating (Friis-Christensen et al. 2006). Swarm-A flies in a circular near-polar orbit with an inclination of 87.35°. For the period under consideration, Swarm-A flew at around 460 km from the ground, crossing the equator at around 08:00 local time (LT) and 20:00 LT, respectively. Notably, previous studies have also used Swarm satellites to assess ionospheric models for satellite applications, benefiting from their precise reference orbits (Montenbruck and González Rodríguez 2020).

GNSS data from Swarm-A was obtained through the ESA platform in the receiver independent exchange format (RINEX), distributed as level 1b products. The dataset includes pseudorange, carrier phase, and signal-to-noise ratio (SNR) measurements collected by a GPS receiver at a frequency of 1 Hz. In addition, we utilized calibrated Slant Total Electron Content (STEC) data, delivered as level 2 products by ESA. Both products are associated to observations by precise orbit determination (POD) antennas on board Swarm satellites (Van den IJssel et al. 2016). To maintain accuracy, we obtained precise ephemerides (SP3) and satellite clock corrections (CLK_30S) of the GPS constellation. These data were acquired through the International GNSS Service (IGS), which provides final products for accurate satellite ephemeris and clock corrections.

Satellite orbit determination with single-frequency gnss data

The primary observations utilized in satellite orbit determination with GNSS are pseudorange and carrier phase. In meters, they are represented as:

$$P = \rho + c(d\tau_r - d\tau_s) + I + \varepsilon_P \tag{1}$$

$$\phi = \rho + C(d\tau_r - d\tau_s) - I + B + \varepsilon_\phi \tag{2}$$

where subscript r represents the GNSS receiver onboard LEO satellites; the subscript s represents the GNSS satellite; P and φ represent the pseudorange and phase of the carrier wave along the line of sight between the GNSS satellite and the onboard receiver; ρ symbolizes the geometric distance along the line of sight; c represents the speed of light in vacuum; $d\tau_r$ and $d\tau_s$ correspond to the clock error in the receiver and GNSS satellite; I is the ionospheric error along the line of sight; B represents the phase ambiguity and remaining biases; and $?_P$ and $?_\varphi$ are the noise errors and other unmodeled terms of the code and phase.

Precise orbit determination (POD) with GNSS typically relies on the ionospheric-free linear combination of two GNSS frequencies, derived from the Eqs. (1) and (2) (Selvan et al. 2023). This combination effectively mitigates most systematic effects of the ionosphere, resulting in accuracy within a few centimeters. However, in the case of single-frequency observations, the ionospheric term needs to be addressed. This is often accomplished by employing an external ionospheric model or by utilizing the GRAPHIC combination.

When ionospheric models are utilized, orbit determination can be directly performed based on Eq. (1) and Eq. (2). Since all other terms can be corrected with satisfactory accuracy, the precision of the orbit determination predominantly relies on the quality of the ionospheric model employed. Consequently, satellite orbit determination using single-frequency GNSS data can serve as a representative measure of the accuracy of the ionospheric model.

Orbit determination using the GRAPHIC observable relies on the fact that ionospheric refraction induces delays in pseudorange measurements (Eq. 1) and advances in carrier phase (Eq. 2). The formulation of this observable is as follows:

$$GRAPHIC = \frac{P+\phi}{2} = \rho + c(d\tau_r - d\tau_s) + \frac{B}{2} + \frac{\varepsilon_p}{2} + \frac{\varepsilon_\phi}{2} \tag{3}$$

where the first-order effect of the ionosphere is eliminated, while ambiguities and noise errors are represented as half of their absolute values.

Numerous works have employed the GRAPHIC observation shown in Eq. (3) for single-frequency orbit determination. Hwang et al. (2011) estimated the orbit solutions for SAC-C and KOMPSAT-2 using single-differenced GRAPHIC observations and a dynamic or reduced dynamic model. Orbital accuracies of about 45 cm and 80 cm were achieved for SAC-C and KOMPSAT-2, respectively. Enderle et al. (2019) obtained an absolute orbit error of about 29 cm with a reduced dynamic model. For APOD-A satellite (Gu et al. 2017), a single-frequency orbit solution of 67.1 cm was obtained using GRAPHIC observables and batch least-squares estimators. Sun et al. (2017a)

implemented a sequential Kalman filter that processes GRAPHIC observations with dynamic orbit models and tested with single-frequency GPS data from SJ-9 A satellite. An accuracy better than 0.50 m was achieved from the internal consistency analysis. In Montenbruck et al. (2005), a position accuracy of 7–8 cm was obtained upon post processing using GRAPHIC observations and a reduced dynamic model based on least-squares for GRACE-B, slightly worse than in the dual-frequency case. In addition, Montenbruck et al. (2012) demonstrated an in-flight precision of 1.1 m 3D root mean square error (RMSE) by utilizing a real-time navigation filter with reduced dynamic model in PROBA-2. Chen et al. (2017) investigated the use of the GRAPHIC observables for single-frequency POD in real-time kinematic positioning, obtaining 3D RMSE accuracy of 75 cm. Sun et al. (2017b) carried out a real-time POD by using single-frequency GPS receiver, GRAPHIC combination, and broadcast ephemeris. A Kalman filter with a reduced dynamic orbit model obtained an accuracy of 46.4 cm, improving the accuracy by about 6 cm compared to the standard Kalman filter.

In this study, we integrate our satellite orbit determination algorithm with an in-house tool named LEO simulator with 9 modules (LEO-S9) (Prol et al. 2024). This tool is primarily designed for simulating LEO satellite missions, offering flexibility in creating various GNSS space segment scenarios, including orbit dynamics and payload instruments. LEO-S9 is optimized for high-precision assessments rather than operational performance. As a result, the single-frequency PPP algorithm integrated into LEO-S9 is implemented through a batch solution. In Eqs. (1), (2), and (3), the unknowns include the LEO satellite positions (x, y, z) and the clock errors ($d\tau_r$) for each epoch, along with a bias term (B) for each satellite arc, assuming no cycle slips or data losses. A rank deficiency arises due to the correlation between clocks and ambiguities. In Eqs. (1) and (2), the clock of the first epoch in each batch solution is estimated using only pseudorange data, allowing the bias term to absorb the clock residual for the first epoch. When using the GRAPHIC observable, the clock error is not estimated in the first epoch, so the clock solution for that epoch is entirely absorbed by the bias term. As a result, the ambiguities incorporated in the bias B are represented as non-integer, or float, values.

Unlike the commonly used Kalman filters, our approach adopts a batch solution to eliminate reliance on prior parameter knowledge and avoid the need of convergence times. Each solution is constructed using 30-minute time intervals. Although the 30-minute data is merged into a single least squares inversion, the satellite position remains unknown for each 1-second epoch. As the main goal is assessing the performance of ionospheric models, we opt for kinematic orbit determination over dynamic or reduced dynamic solutions. This decision aims to prevent residuals from being absorbed by other parameters, such as solar radiation pressure or empirical accelerations in radial, along-track, or cross-track components. Consequently, our evaluation ensures that the performance analysis focuses on the quality of the ionospheric models without interference from other-related models. The adopted approach results in several arcs with inconsistent outcomes. All arcs in which either the GRAPHIC or reference PPP solution exhibited large residuals are excluded from the analysis, leading to the removal of 30% of the arcs. This approach ensures that the ionospheric models are evaluated using only the PPP or GRAPHIC results with the highest accuracy. GNSS satellite corrections are acquired through precise IGS files for ephemeris, clocks, and antenna calibration parameters. All observables are related to the GPS frequency in the L1 band for single-frequency PPP. Additionally, we conduct the same analysis using dual-frequency PPP (L1/L2) to obtain a reference benchmark.

Ionospheric models

Ionospheric modeling has been a topic of active research since the 1960s. A variety of models reproducing electron density distributions have been developed, some of them covering the entire electron density profiles from the D-region up to the plasmasphere, such as the International Reference Ionosphere (IRI) (Bilitza et al. 2022), while others targeting more specific regions, such as the topside ionosphere (Bilitza and Xiong 2021; Smirnov et al. 2023). Some of the most established global models include the IRI, NeQuick (Nava et al. 2008), and the NEDM (Hoque et al. 2022). One advantage of the global 3D models lies in their suitability for ground-based PPP, as well as for satellite orbit determination from single-frequency GNSS data. At the same time, a global 3D electron density modeling is generally a more challenging task compared to representing the ionospheric plasma for specific regions. Therefore, models which cover all altitude ranges and regions of the ionosphere-plasmasphere system might come with a certain degree of smoothing and tend towards a more general climatological representation of electron densities. On the other hand, the local models, such as the recent Neural network model of Electron density in Earth's Topside ionosphere (NET) (Smirnov et al. 2023) together with its plasmaspheric extension (Prol et al. 2022), have been shown to reproduce in-situ observations of several LEO missions with very high accuracy.

Three ionospheric model strategies are utilized in this study to correct the ionospheric errors for satellite orbit determination. They are described as follows:

- **Climatological model**: The 3D electron density model NEDM2020 (Hoque et al. 2022) is developed by combining Chapman layers representing the ionospheric F-layer and E-layer, and a plasmasphere model. The topside ionosphere and plasmasphere is established by superposing the Neustrelitz Plasmasphere Model (NPSM) (Jakowski and Hoque 2018) to the F-layer and E-layer models. The model uses a limited number of model coefficients (< 100) with no interpolation technique. Therefore, NEDM2020 is a fast-running model and suitable for operational purpose.
- **Ionospheric Tomography**: The solutions derived by Prol et al. (2021a) were directly employed in the current study. These solutions correspond to a global tomography framework designed to process data from over 2,700 GNSS stations. The tomography method utilized the algebraic reconstruction technique (ART) to invert STEC data into electron density (N_e). Additionally, VTEC data was incorporated to ensure alignment with the latest accuracy trends (Zheng et al. 2021). The NEDM served as the background model. We adopted a spatial resolution of 2° × 2° × 20 km for latitude, longitude, and altitude, respectively. The vertical distribution ranges from 50 to 20,000 km, from the ionosphere bottomside to the GNSS orbit height in the plasmasphere. A time resolution of 15 min was defined, necessitating 96 runs for a daily tomography.
- **Iono OFF**: This solution is applied without correcting for the ionospheric delay, i.e., ionospheric models are disabled. This is analyzed to provide a clear view of the actual improvements offered by the ionospheric models.

For visualization purposes of the Swarm data, we have developed a Swarm VTEC model derived from calibrated STEC values processed by ESA. The Swarm VTEC model was developed with a procedure similar to the one carried out by Prol et al. (2021b); Prol and Hoque (2022). In these previous works, it was found that when superimposing LEO satellite data collected during the rising or setting orbit phases, daily measurements cover the entire globe with a repetitive pattern in terms of local time. It is therefore possible to superimpose the TEC data of the entire day and represent the ionosphere with two grids: during nighttime and daytime. Since the model is based on a single satellite, it offers limited observations of the spatial and temporal variability of the ionosphere. Due to this limitation, the PPP evaluation is not performed using this Swarm VTEC model. We only use it to understand how the ionosphere has been seen by the Swarm-A satellite. The observed STEC values were converted to VTEC ones using the mapping function proposed by Foelsche and Kirchengast (2002), assuming a single-shell height of 1,000 km. Figure 1 shows the geometric schematic used to derive VTEC data. This mapping function was selected to keep equal standards to previous works developed by Prol et al. (2023). Surface modeling was accomplished using the spherical harmonic (SH) function developed by Prol et al. (2022). The input VTEC values were represented in terms of LT, with the SH coefficients determined through a least squares adjustment for each day independently. Consistent with Prol and Hoque (2022), two models were established for each day: one for LT < = 12 and another one for LT > 12, thereby distinguishing between satellite rising and setting phases.

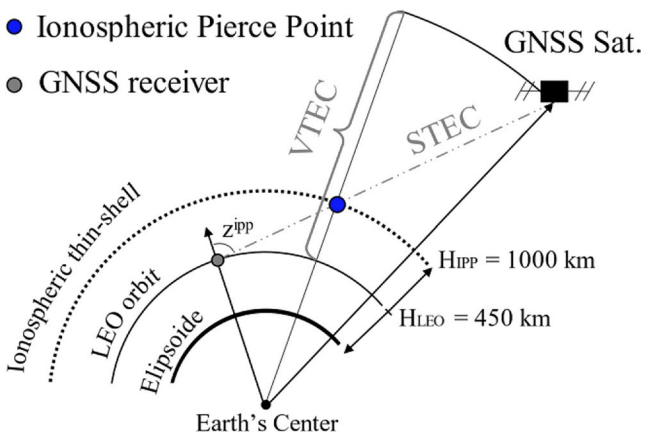

Fig. 1 Geometric illustration utilized to compute VTEC values between LEO and GNSS satellites at the ionospheric pierce point (IPP), where z and H represent the zenith angle and the altitude, respectively

Results and discussion

Storm event and data quality

Figure 2 illustrates VTEC maps generated by the three models under examination. Figure 3 depicts the progression of the geomagnetic storm as represented by the SYM-H index, marking the storm's intensity at the time points corresponding to the daytime VTEC maps. The Swarm VTEC model considers the geometry of the Swarm-A satellite. Since this model is developed solely from Swarm TEC data, two distinct 2D grids are employed to represent the TEC data for the entire day: one for the satellite's ascending track and another one for the satellite's descending track. These 2D grids are constructed in latitude and longitude coordinates and specifically developed to show only ionospheric variabilities above the satellite locations. Consequently, the Swarm model's VTEC representation is limited to show the LTs during which the satellite collects data, simplified here as daytime and nighttime. In the case of NEDM and tomography (TOMO), VTEC data was obtained by integrating electron density data from the Swarm-A orbit height up to the GPS altitude. Noticeable differences are observed

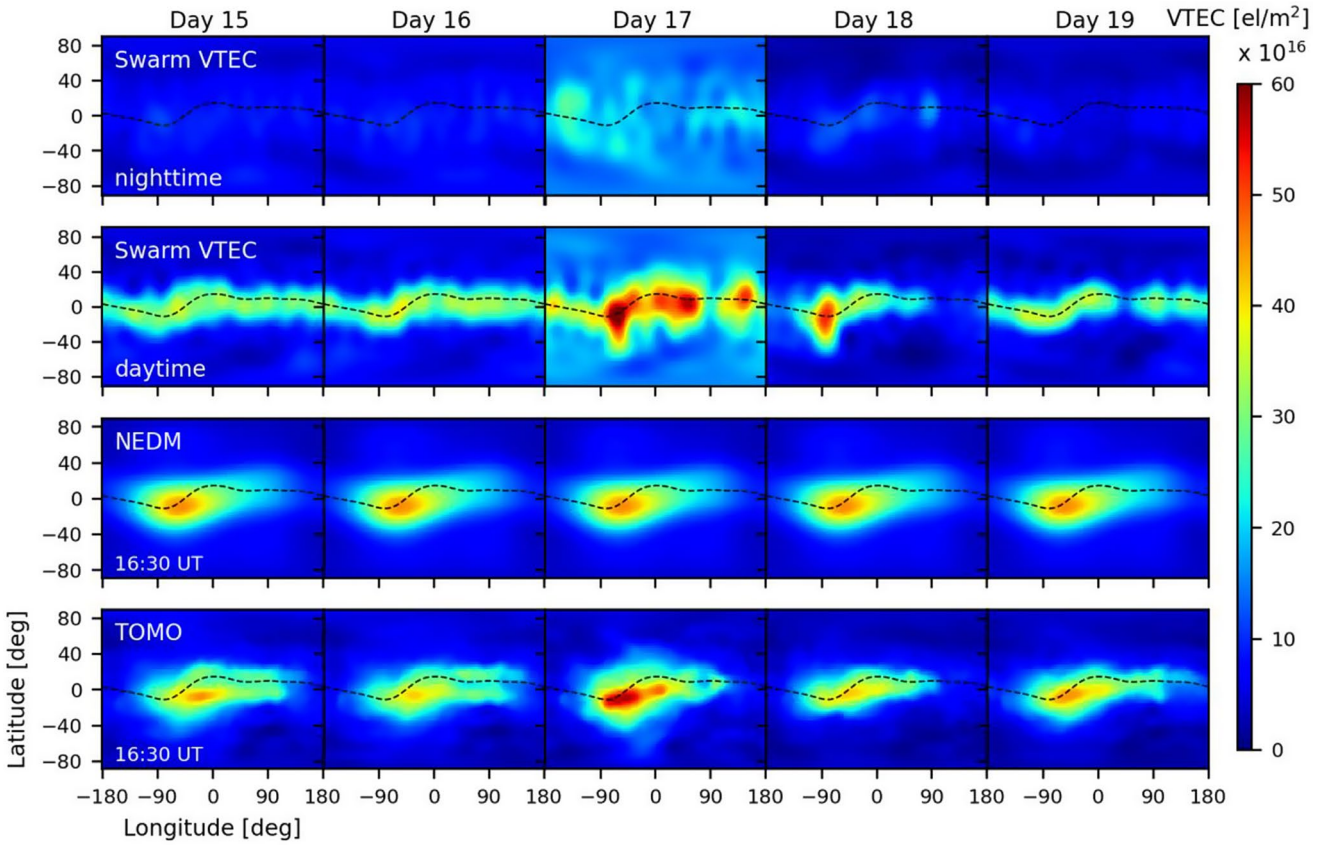

Fig. 2 VTEC maps obtained with the three models under evaluation. VTEC values account from 450 km up to the GPS altitudes. Top two panels represent the maps obtained with daily averages of the VTEC model based on Swarm-A data recorded during nighttime and daytime. Mid panels are related to the NEDM model at 16:30 h UT. Bottom panels refer to the maps obtained with the tomographic model at 16:30 h UT. Black dashed lines represent the geomagnetic equator

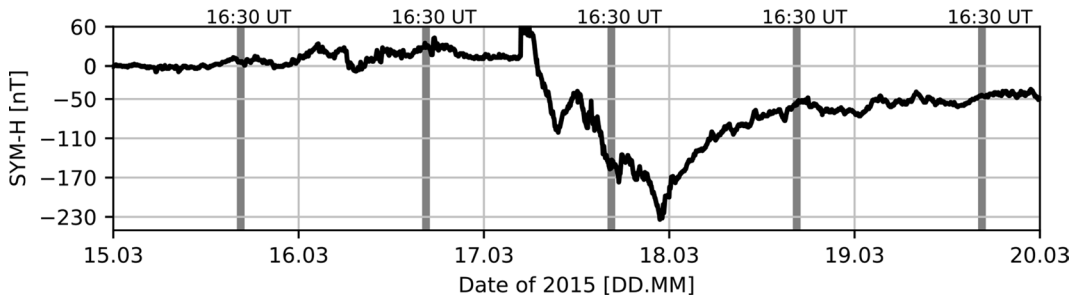

Fig. 3 SYM-H index provided the Goddard Space Flight Center in the OMNI data set. Gray lines indicated the SYM-H values at the instances analyzed in Fig. 1

among the representations. The Swarm VTEC model exhibits enhanced structures near the equatorial region, while the TOMO model shows signatures of the crests of the equatorial ionization anomaly (EIA). This disparity arises because the Swarm VTEC model is only based on GNSS receivers onboard LEO satellites, while TOMO utilize ground-based GNSS data. In contrast to both, NEDM represents monthly average TEC values which smooths out daily variations. The Swarm VTEC model and TOMO results also reveal displacements of the EIA crests on day 17th of March, which is consistent with what was found by Pignalberi et al. (2016) by analyzing electron density values from Swarm-A and -B. This displacement is attributed to the impact of the St. Patrick Storm 2015, associated with the penetration of eastward electric fields into the daytime ionosphere, that caused a "super-fountain effect" (e.g., Zong et al. 2010). A significant inhibition of EIA formation is observed during the recovery phase on day 18th of March. The negative effects of the St. Patrick storm, commonly attributed to disturbance dynamo electric field and westward motions, are

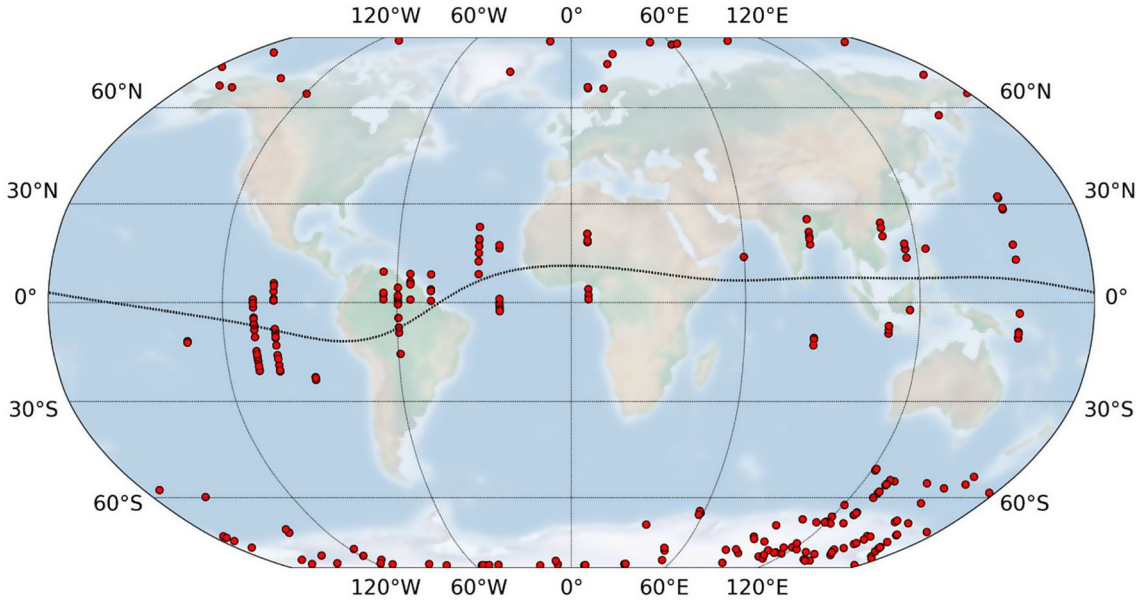

Fig. 4 Spatial distribution of GPS LoLs (red dots) experienced by Swarm A in the period 14 – 20 March 2015

Table 1 Number of LoL events experienced by Swarm A for each day of the period 14 – 20 March 2015

Day of March 2015	14	15	16	17	18	19	20
LoLs counts	46	43	18	118	4	29	24

well-documented in the literature (e.g., Borries et al. 2016; Spogli et al. 2016).

The NEDM does not include any geomagnetic activity dependence in the numerical coefficients used to model the ionosphere. Consequently, NEDM VTEC values have no time variation among different days. Differently, TOMO model takes advantage from the assimilation of STEC observations to improve both the spatial and time description of the background NEDM model. This is particularly evident under disturbed conditions (17th of March), where the largest differences between the two models are appreciable. The representation of plasma variations driven by geomagnetic activity in ionospheric empirical climatological models is still a challenge.

On the storm day, the Swarm VTEC model shows a sudden jump. To assess its impact on the Swarm positioning data, we evaluate in Fig. 4 the number of losses of lock (LoLs) over GPS satellites. By design, Swarm POD antennas can track at most eight GPS satellites in the field of view, but this number is affected by geometrical factors and by other related effects of the radio signals propagating in the ionosphere. Pezzopane et al. (2021) used 7 years of Swarm satellites STEC data to identify LoLs and investigated their main spatial and temporal patterns. By applying the same methodology, we identified 282 LoL events in Swarm-A STEC data for the period under consideration. Table 1 shows that the occurrence of LoL events maximize during the main phase of the storm on 17th March, while they decrease sharply in the other days. This is consistent with the findings by Lovati et al. (2023) that highlighted a sharp increase in LoL events under geomagnetically disturbed conditions due to the establishment of small-scale plasma irregularities (De Michelis et al. 2022). As a result, we anticipate data modeling challenges primarily at high and low latitudes, leading to lower positioning performance in the polar regions and near the geomagnetic equator.

Accuracy of the orbit determination

Figure 5 illustrates the average error of the single-frequency PPP batch solutions on a representative day of a quiet ionosphere. Each batch solution comprises 30 min of observations. The average errors are computed in the 3D component of the coordinates, using the PPP solution with double-frequency GPS signals as a benchmark, i.e., PPP with ionospheric-free observations serves as a reference for accuracy evaluation. It is evident that the lowest accuracy was observed when no ionospheric model was used, followed by the climatological model NEDM, the tomographic approach, and the technique employing GRAPHIC observables. Notably, our analysis demonstrates that the batch solution approach has provided a stable accuracy over each arc of 30 min. This implies that all processed data can be evaluated without considering PPP convergence times, typical in a Kalman Filter PPP algorithm. Additionally, there is no need to account for reinitialization processes during

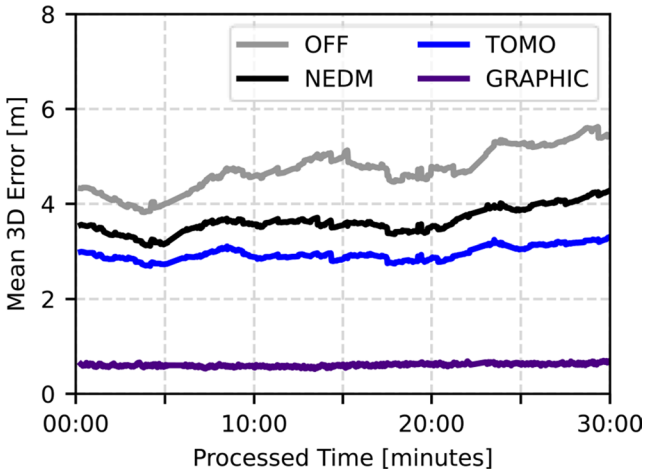

Fig. 5 Average error of the 30-minute arcs formed to process the batch solutions of the orbit determination technique during March 15, 2015. Errors were computed using single-frequency GNSS data with the GRAPHIC observable and raw L1 observables corrected by ionospheric models. Dual-frequency PPP is used as the reference benchmark

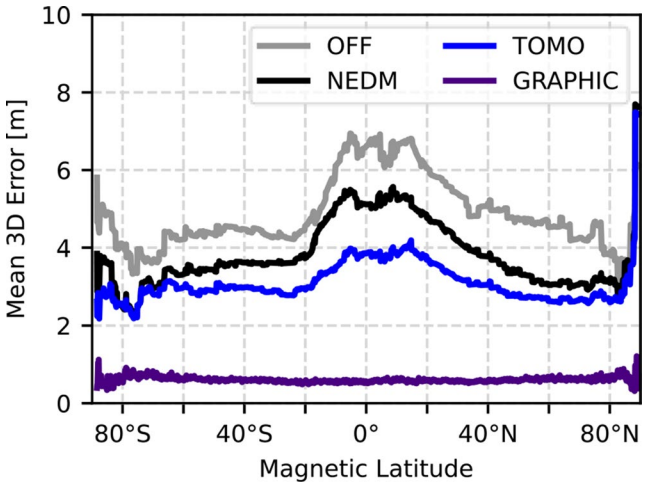

Fig. 6 Same as Fig. 5, but the average errors are now plotted as a function of the magnetic latitude

instances of GPS loss of lock, allowing all epochs to be used for accuracy evaluation.

Figure 6 shows the average errors of the single-frequency PPP solutions plotted against the magnetic latitude. The GRAPHIC solution exhibits consistency across the magnetic latitudes, with slightly diminished performance in polar regions. The lower performance can be attributed to the increased frequency of signal losses and reduced GPS visibility at higher latitudes, because of the orbital inclination of approximately 55°. The solutions depending on the ionospheric models, on the other hand, are influenced by the ionosphere. A decreased performance is mainly observed in low latitudes. Specifically, the performance of NEDM and tomographic models lowers at the equatorial regions, reaching its lowest at a magnetic latitude of around $\pm 10°$. A notable performance increase is observed when transitioning to mid-latitudes. A similar pattern is observed when ionospheric models are turned off, but with a noticeable decrease in accuracy compared to the NEDM and TOMO models.

In Fig. 7 (left panel), the average accuracy of single-frequency PPP solutions is plotted as a function of local time. Once more, the GRAPHIC solution demonstrates consistent performance, showing resilience to ionospheric dynamics. The PPP solutions depending on ionospheric models are notably influenced by the local time. However, this distribution alone does not fully elucidate the factors affecting the performance; it is necessary to analyze the satellite orbit trajectory (right panel) in conjunction. The best accuracies are observed during nighttime, particularly in high latitude regions. In high latitudes, NEDM shows a stable accuracy in the daytime, with slightly worse performance at the nighttime. TOMO results present the most stable solution within LTs. Only near 90° in latitude does the accuracy diminishes in all methods, primarily due to decreased visibility of GPS satellites. This discrepancy is more pronounced when ionospheric models are off. As the satellite traverses the equatorial region, positioning accuracy diminishes, with the lowest accuracies recorded around 8 h and 20 h LT, precisely when

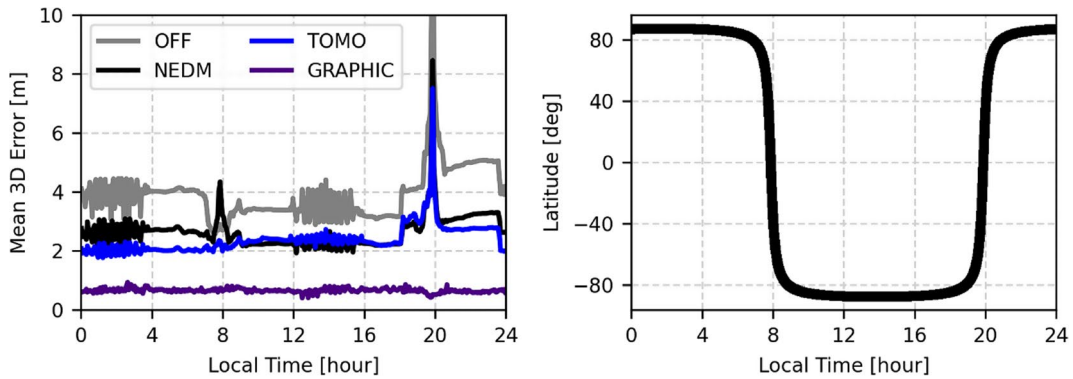

Fig. 7 The left panel shows the same as Fig. 5, but the average errors are now plotted as a function of the local time. The right panel shows the footprint of the Swarm-A satellite orbit

the satellite crosses the equator. The tomography model demonstrated consistency across different local times and latitudes. However, it is notably impacted in the equatorial region around 20 h LT. The most significant discrepancy in tomographic modeling appears to be associated with the transition from daytime to nighttime in the equatorial region when ionospheric irregularities are prominent at low latitudes. At those LTs, complex electrodynamics, caused by the pre-reversal enhancements (Woodman 1970), take control of the ionosphere, leading to the formation of ionospheric irregularities. Additionally, jumps occur around 24 h LT, primarily attributed to model artifacts that originate from the absence of a smooth transition between the days.

Figure 8 shows the 3D errors of the solutions across all analyzed days, plotted against the hours of each day in UT. The color bars' maximum and minimum ranges vary within each method to make it easier to the reader to visualize. No discernible trend is evident. The accuracy is dispersed around the average accuracy of each method, with maximum errors reaching 2.5 m for GRAPHIC, 12.0 m for NEDM, 12.0 m for TOMO, and 25.0 m when ionospheric models are off. A remarkable trend is only noticed in March 17, where every method exhibits reduced accuracy compared to other days. This is attributed to challenges in representing the ionosphere under severe geomagnetic conditions. On average, during non-stormy days, the 3D error is 0.59 m for GRAPHIC, 3.55 m for NEDM, 2.80 m for TOMO, and 4.86 m for the OFF. Conversely, during storm conditions, the average 3D error increased to 0.92 m for GRAPHIC, 4.30 m for NEDM, and 4.00 m for TOMO, and 6.39 m for OFF. This highlights that ionospheric models led to an average 40% reduction in performance during storm days.

Figure 9 shows the cumulative percentage of cases of the 3D errors over the whole period of 14 – 20 March 2015. This result reveals the frequency with which positioning strategies fall within specific accuracy ranges. For example, the GRAPHIC solution consistently achieves sub-meter accuracy 80% of the time, with maximum errors of approximately 2 m. The tomographic solution maintains a 4-meter accuracy level 80% of the time. Similarly, the NEDM model allows a 5-meter accuracy 80% of the time, whereas the OFF option yields approximately 7 m accuracy within the same

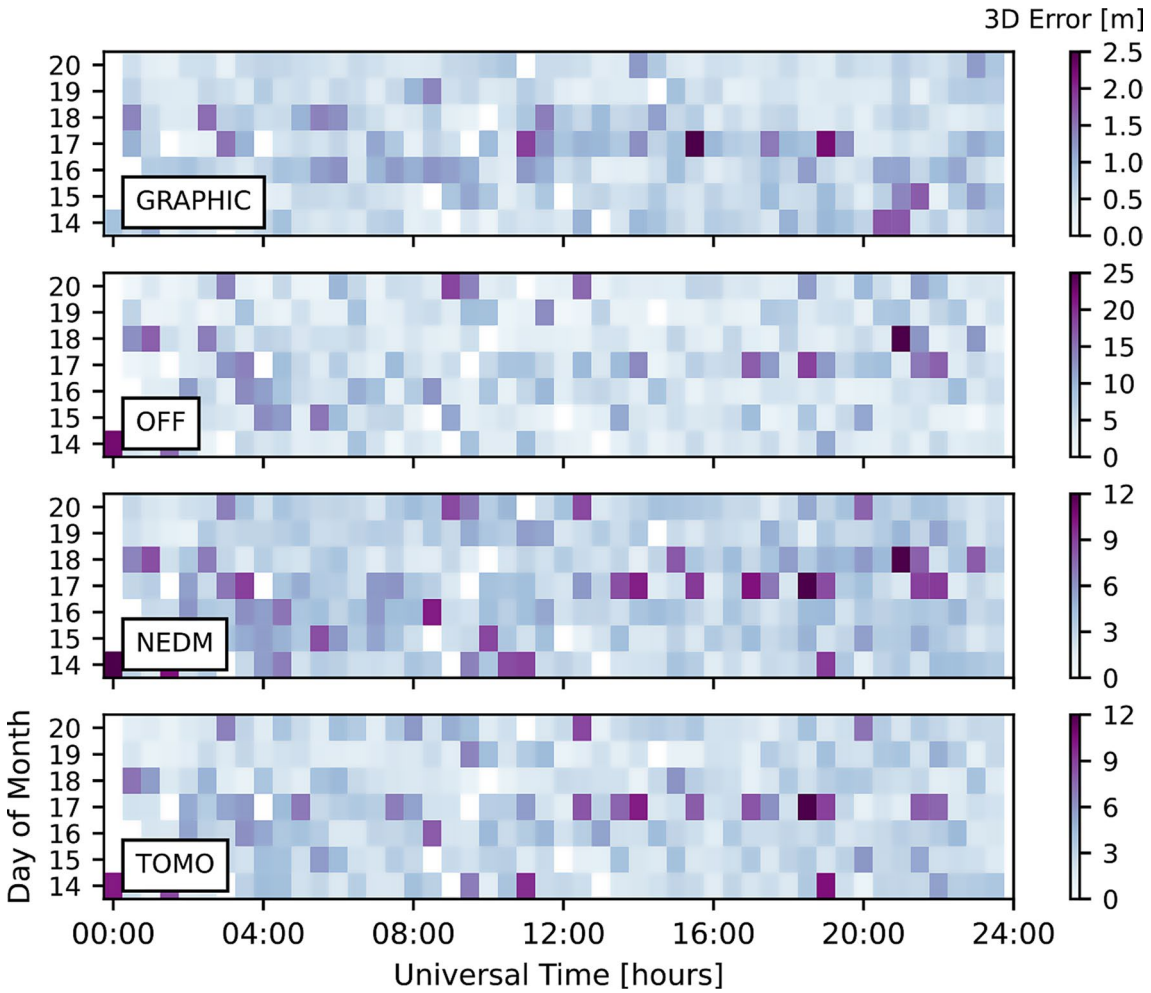

Fig. 8 Average error distributions as a function of the hour of the day and day of the month

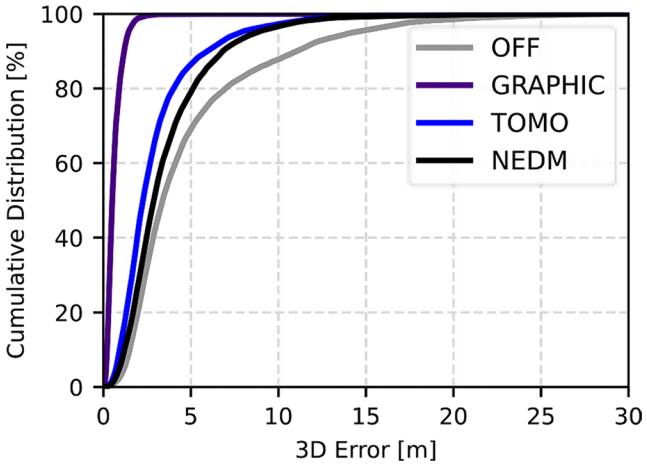

Fig. 9 Cumulative distribution of the average error in each positioning mode. All days under evaluation are considered

Table 2 Absolute mean (μ), standard deviation (σ), and RMSE of the 3D errors obtained with distinct positioning modes. The whole period of 14–20 March 2015 is considered

Positioning Mode	Mean 3D Error [m]	Std. Deviation 3D Error [m]	3D RMSE [m]
Iono OFF	5.00	4.60	6.79
NEDM	3.62	2.73	4.53
TOMO	2.97	2.45	3.85
GRAPHIC	0.62	0.47	0.78

percentage of cases. Maximum errors for tomography and NEDM remain around 12 m, while the OFF option shows maximum errors of around 20 m.

Table 2 summarizes the accuracy achieved in all days analyzed. The performance is presented in terms of average, standard deviation, and RMSE. The PPP processing strategy without ionospheric model presents the worst solution, with a total RMSE of around 6.79 m. The NEDM and tomography results present a slighted biased solution of around 3.5 m and 3 m and a RMSE of around 4.5 and 3.8 m, respectively. This outcome again highlights the effectiveness of tomography to correctly update the background distributions. The GRAPHIC solution provides the best performance, with a RMSE of 0.78 m, and is consistent with the findings of Hwang et al. (2011), Gu et al. (2017), and Chen et al. (2017).

Conclusions

We have demonstrated the capabilities of global-scale tomography in performing satellite orbit determination using single-frequency GNSS data. A comprehensive dataset of STEC values obtained from ground-based GNSS receivers was utilized to conduct tomography over a week impacted by the St. Patrick's Day geomagnetic storm in 2015. Compared to the background model, tomography exhibited improvements of approximately 18% in the mean 3D error and 16% in RMSE. This behavior was consistent across various latitudes and local times, indicating a systematic improvement made by the tomography approach. Specifically, tomography achieved an average accuracy of 2.8 m for quiet days, which reduces by about 40% during storm days. Furthermore, compared to a single-frequency PPP solution without ionospheric corrections, the tomography method improved orbit determination accuracy by approximately 50%.

The developed tomography technique requires prohibitively long processing times for extended time series. Hence, we recommend future advancements to optimize this technique, allowing for the extension of our analysis across different seasons and solar cycles. The analysis initiated for the St. Patrick's Day geomagnetic storm can also be extended to other extreme events, systematically assessing the accuracy of 3D ionospheric models for orbit determination under different disturbed conditions. Furthermore, further tomography optimizations might enable the expansion of this preliminary evaluation by means of the inclusion of multiple LEO satellites, taking into account distinct orbital altitudes.

Despite considerable efforts to enhance ionospheric modeling, the experimental models evaluated in our study still exhibit lower performance in orbit determination compared to GRAPHIC observables. Thus, there is a wide opportunity for improving ionospheric models with the aim of surpassing GRAPHIC solutions. For better performance, higher-resolution tomography approaches are necessary, requiring the integration of space- and ground-based GNSS data. This aligns with recommendations made by Han et al. (2022) and Schreiter et al. (2024), emphasizing the importance of dense satellite constellations at LEO altitudes, even considering the risk of increased computational strain in the processing phase.

Acknowledgements The authors would like to acknowledge the Joint Study Group 1 'Understanding Ionospheric and Plasmaspheric Processes' of the GGOS (Global Geodetic Observing System) Focus Area on Geodetic Space Weather Research (GSWR) for their support and collaboration.

Author contributions F.S.P and A.P wrote the main manuscript text and prepared figures. A.S, M.P, A.L.C., and K.S. helped in the analysis with satellite orbit determination and ionospheric modelling results. M.H. developed the model used as background for tomography (NEDM). F.S.P and S.K. are responsible for the project funding. All authors reviewed the manuscript.

Funding This work was supported in part by the Research Council of Finland under the project "Exploring the Upper Limits of the Ionosphere" (EULI), under decision number 362096, and in part by the

INdoor Navigation from CUBesAT Technology (INCUBATE) project, funded by the Technology Industries of Finland Centennial Foundation and the Jane and Aatos Erkko Foundation (JAES). Open Access funding was provided by the National Land Survey of Finland.
Open Access funding provided by National Land Survey of Finland.

Data availability No datasets were generated or analysed during the current study.

Declarations

Ethical approval The authors declare no competing interests.

Competing interests The authors declare no competing interests.

References

Aa E, Forsythe VV, Zhang S-R, Wang W, Coster AJ (2023) Next-decade needs for 3-D ionosphere imaging. Front Astron Space Sci 10:1186513. https://doi.org/10.3389/fspas.2023.1186513

Balan N, Shiokawa K, Otsuka Y, Kikuchi T, Vijaya Lekshmi D, Kawamura S, Yamamoto M, Bailey GJ (2010) A physical mechanism of positive ionospheric storms at low latitudes and midlatitudes. J Geophys Res 115:A02304. https://doi.org/10.1029/2009JA014515

Bilitza D, Xiong C (2021) A solar activity correction term for the IRI topside electron density model. Adv Space Res 68:2124–2137. https://doi.org/10.1016/j.asr.2020.11.012

Bilitza D, Pezzopane M, Truhlik V, Altadill D, Reinisch BW, Pignalberi A (2022) The International Reference Ionosphere model: a review and description of an ionospheric benchmark. Rev Geophys 60. https://doi.org/10.1029/2022RG000792. e2022RG000792

Bock H, Jäggi A, Dach R, Schaer S, Beutler G (2009) GPS single-frequency orbit determination for low Earth orbiting satellites. Adv Space Res 43:783–791. https://doi.org/10.1016/j.asr.2008.12.003

Borries C, Mahrous AM, Ellahouny NM, Badeke R (2016) Multiple ionospheric perturbations during the Saint Patrick's Day storm 2015 in the european-african sector. J Geophys Research: Space Phys 121:11333–11345. https://doi.org/10.1002/2016JA023178

Chen P, Zhang J, Sun X (2017) Real-time kinematic positioning of LEO satellites using a single-frequency GPS receiver. GPS Solutions 21:973–984. https://doi.org/10.1007/s10291-016-0586-1

Chen CH, Lin CCH, Lee CJ, Liu JY, Saito A (2022) Ionospheric responses on the 21 August 2017 solar eclipse by using three-dimensional GNSS tomography. Earth Planet Space 74:173. https://doi.org/10.1186/s40623-022-01734-y

Chen Y, Yue D, Zhai C (2024) Study on four-dimensional evolution of concentric traveling ionospheric disturbances after Falcon 9 Rocket Launch using Ionospheric Tomography. IEEE J Sel Top Appl Earth Observations Remote Sens 17:377–387. https://doi.org/10.1109/JSTARS.2023.3329203

Conrad AV, Axelrad P, Haines B, Zuffada C, O'Brien A (2023) Improved GPS-based single-frequency orbit determination for the CYGNSS spacecraft using GipsyX. https://doi.org/10.33012/navi.565. Navigation 70

De Michelis P, Consolini G, Pignalberi A, Lovati G, Pezzopane M, Tozzi R, Giannattasio F, Coco I, Marcucci MF (2022) Ionospheric turbulence: a challenge for GPS loss of lock understanding. Space Weather 20:e2022SW003129. https://doi.org/10.1029/2022SW003129

Dong-Ju P, Bin W (2012) The application of GIM in precise orbit determination for LEO satellites with single-frequency GPS measurements. Chin Astron Astrophy 36:366–381. https://doi.org/10.1016/j.chinastron.2012.10.002

Enderle W, Gini F, Schönemann E, Mayer V (2019) PROBA-3 Precise Orbit determination based on GNSS observations. Proc 32nd Int Tech Meeting Satell Div Inst Navig (ION GNSS + 2019) 1187–1198. https://doi.org/10.33012/2019.17083. Miami, Florida, September

Foelsche U, Kirchengast GA (2002) Simple geometric mapping function for the hydrostatic delay at radio frequencies and assessment of its performance. Geophys Res Lett 29:111. https://doi.org/10.1029/2001GL013744. 1-111–4

Forootan E, Kosary M, Farzaneh S, Schumacher M (2023) Empirical Data Assimilation for Merging Total Electron Content Data with empirical and physical models. Surv Geophys 44:2011–2041. https://doi.org/10.1007/s10712-023-09788-7

Friis-Christensen E, Lühr H, Hulot G (2006) Swarm: a constellation to study the Earth's magnetic field. Earth Planet Sp 58:351–358. https://doi.org/10.1186/BF03351933

Garcia-Fernàndez M, Montenbruck O (2006) Low Earth orbit satellite navigation errors and vertical total electron content in single-frequency GPS tracking. Radio Sci 41:RS5001. https://doi.org/10.1029/2005RS003420

Gu D, Liu Y, Bin Y, Cao J, Xie L (2017) In-flight performance analysis of MEMS GPS receiver and its application to precise orbit determination of APOD-A satellite. Adv Space Res 60:2723–2732. https://doi.org/10.1016/j.asr.2017.08.023

Guo J, Qi L, Liu X, Chang X, Ji B, Zhang F (2023) High-order ionospheric delay correction of GNSS data for precise reduced-dynamic determination of LEO satellite orbits: cases of GOCE, GRACE, and SWARM. GPS Solut 27:13. https://doi.org/10.1007/s10291-022-01349-6

Han Y, Wang L, Chen R, Fu W, Li T, Zhou H (2022) Toward real-time construction of global ionosphere map from ground and space-borne observations. GPS Solut 26:147. https://doi.org/10.1007/s10291-022-01337-w

Hoque MM, Jakowski N, Prol FS (2022) A new climatological electron density model for supporting space weather services. J Space Weather Space Clim 12:1. https://doi.org/10.1051/swsc/2021044

Hwang Y, Lee B-S, Kim H, Kim J (2011) Orbit determination performances using single- and double-differenced methods: SAC-C and KOMPSAT-2. Adv Space Res 47:138–148. https://doi.org/10.1016/j.asr.2010.07.027

Jakowski N, Hoque MM (2018) A new electron density model of the plasmasphere for operational applications and services. J Space Weather Space Clim 8:A16. https://doi.org/10.1051/swsc/201802

Kamide Y, Kusano K (2015) No major solar flares but the largest geomagnetic storm in the Present Solar cycle. Space Weather 13:365–367. https://doi.org/10.1002/2015SW001213

Karki B, Won M (2020) Characterizing Power Consumption of Dual-Frequency GNSS of Smartphone. In GLOBECOM 2020, IEEE Global Communications Conference, Taipei, Taiwan, pp. 1–6

Kovář P (2017) piNAV L1—GPS receiver for small satellites. Gyroscopy Navig 8:159–164. https://doi.org/10.1134/S2075108717020079

Long Y, Huo X, Liu H, Li Y, Sun W (2023) An Extended Simultaneous Algebraic Reconstruction technique for imaging the Ionosphere using GNSS Data and its preliminary results. Remote Sens 15:2939. https://doi.org/10.3390/rs15112939

Lovati G, De Michelis P, Consolini G, Pezzopane M, Pignalberi A, Berrilli F (2023) Decomposing solar and geomagnetic activity and seasonal dependencies to examine the relationship between GPS loss of lock and ionospheric turbulence. Sci Rep 13:9287. https://doi.org/10.1038/s41598-023-34727-2

Mei D, Ren X, Liu H, Le X, Xiong S, Zhang X (2023) Global three-dimensional ionospheric tomography by combination of ground-based and space-borne GNSS data. Space Weather 21. https://doi.org/10.1029/2022SW003368. e2022SW003368

Montenbruck O (2003) Kinematic GPS positioning of LEO satellites using ionosphere-free single frequency measurements. Aerosp Sci Technol 7:396–405. https://doi.org/10.1016/S1270-9638(03)00034-8

Montenbruck O, González Rodríguez B (2020) NeQuick-G performance assessment for space applications. GPS Solut 24:13. https://doi.org/10.1007/s10291-019-0931-2

Montenbruck O, Helleputte T, Kroes R, Gill E (2005) Reduced dynamic orbit determination using GPS code and carrier measurements. Aerosp Sci Technol 9:261–271. https://doi.org/10.1016/j.ast.2005.01.003

Montenbruck O, Swatschina P, Markgraf M, Santandrea S, Naudet J, Tilmans E (2012) Precision spacecraft navigation using a low-cost GPS receiver. GPS Solutions 519–529. https://doi.org/10.1007/s10291-011-0252-6

Müller L, Chen K, Möller G, Rothacher M, Soja B, Lopez L (2024) Real-time navigation solutions of low-cost off-the-shelf GNSS receivers on board the Astrocast constellation satellites. Adv Space Res 73:2–19. https://doi.org/10.1016/j.asr.2023.10.001

Nava B, Coisson P, Radicella SM (2008) A new version of the NeQuick ionosphere electron density model. J Atmos Solar Terr Phys 70:1856–1862. https://doi.org/10.1016/j.jastp.2008.01.015

Norberg J, Käki S, Roininen L, Mielich J, Virtanen II (2023) Model-free approach for regional ionospheric multi-instrument imaging. J Geophys Research: Space Phys 128. https://doi.org/10.1029/2022JA030794. e2022JA030794

Pezzopane M, Pignalberi A, Coco I, Consolini G, De Michelis P, Giannattasio F, Marcucci MF, Tozzi R (2021) Occurrence of GPS loss of lock based on a Swarm Half-Solar cycle dataset and its relation to the background Ionosphere. Remote Sens 13:2209. https://doi.org/10.3390/rs13112209

Pignalberi A, Pezzopane M, Tozzi R, De Michelis P, Coco I (2016) Comparison between IRI and preliminary Swarm Langmuir probe measurements during the St. Patrick storm period. Earth Planet Space 68:93. https://doi.org/10.1186/s40623-016-0466-5

Pokhotelov D, Fernandez-Gomez I, Borries C (2021) Polar tongue of ionisation during geomagnetic superstorm. Ann Geophys 39:833–847. https://doi.org/10.5194/angeo-39-833-2021

Prol FS, Hoque MM (2022) A Tomographic Method for the Reconstruction of the Plasmasphere based on COSMIC/ FORMOSAT-3 data. IEEE J Sel Top Appl Earth Observations Remote Sens 15:2197–2208. https://doi.org/10.1109/JSTARS.2022.3155926

Prol FS, Hoque MM, Ferreira AA (2021a) Plasmasphere and topside ionosphere reconstruction using METOP satellite data during geomagnetic storms. J Space Weather Space Clim 11:5. https://doi.org/10.1051/swsc/2020076

Prol FS, Kodikara T, Hoque MM, Borries C (2021b) Global-scale ionospheric tomography during the March 17, 2015 geomagnetic storm. Space Weather 19. https://doi.org/10.1029/2021SW002889. e2021SW002889

Prol FS, Smirnov AG, Hoque MM, Shprits YY (2022) Combined model of topside ionosphere and plasmasphere derived from radio-occultation and Van Allen Probes data. Sci Rep 12:9732. https://doi.org/10.1038/s41598-022-13302-1

Prol FS, Smirnov A, Kaasalainen S, Hoque MM, Bhuiyan MZH, Menzione F (2023) The potential of LEO-PNT mega-constellations for Ionospheric 3-D imaging: a Simulation Study. IEEE J Sel Top Appl Earth Observations Remote Sens 16:7559–7571. https://doi.org/10.1109/JSTARS.2023.3299415

Prol FS, Zahidul MHB, Kaasalainen S, Lohan ES, Praks J, Çelikbilek K, Kuusniemi H (2024) Simulations of Dedicated LEO-PNT Systems for Precise Point Positioning: Methodology, Parameter Analysis, and Accuracy Evaluation. IEEE Transactions on Aerospace and Electronic Systems, In Press. https://doi.org/10.1109/TAES.2024.3404909

Qi L, Guo J, Xia Y, Yang Z (2021) Effect of higher-order ionospheric delay on precise orbit determination of GRACE-FO based on satellite-borne GPS technique. IEEE Access 9:29841–29849. https://doi.org/10.1109/ACCESS.2021.3059296

Schreiter LF, Brack A, Männel B, Schuh H, Arnold D, Jäggi A (2024) Imaging of the topside ionosphere using GNSS slant TEC obtained from LEO satellites. ESS Open Archive January 24. https://doi.org/10.22541/essoar.170612533.38060840/v1

Selvan K, Siemuri A, Prol FS, Välisuo P, Zahidul MHB, Kuusniemi H (2023) Precise orbit determination of LEO satellites: a systematic review. GPS Solut 27:178. https://doi.org/10.1007/s10291-023-01520-7

Shan LL, Yao YB, Kong J, Zhai CZ, Zhou C, Chen XX (2022) Three-dimensional reconstruction of tongue of ionization during the 11 October 2010 geomagnetic storm and evolution analysis with TIEGCM. Space Weather 20:e2021SW002862. https://doi.org/10.1029/2021SW002862

Smirnov A, Shprits Y, Prol F, Lühr H, Berrendorf M, Zhelavskaya I, Xiong C (2023) A novel neural network model of Earth's topside ionosphere. Sci Rep 13:1303. https://doi.org/10.1038/s41598-023-28034-z

Spogli L et al (2016) Formation of ionospheric irregularities over Southeast Asia during the 2015 St. Patrick's Day storm. J Geophys Res Space Phys 121:12211–12233. https://doi.org/10.1002/2016JA023222

Sun X, Han C, Chen P (2017a) Precise real-time navigation of LEO satellites using a single-frequency GPS receiver and ultra-rapid ephemerides. Aerosp Sci Technol 67:228–236. https://doi.org/10.1016/j.ast.2017.04.006

Sun X, Han C, Chen P (2017b) Real-time precise orbit determination of LEO satellites using a single-frequency GPS receiver: preliminary results of Chinese SJ-9A satellite. Adv Space Res 60:1478–1487. https://doi.org/10.1016/j.asr.2017.06.052

Tsagouri I, Themens DR, Belehaki A, Shim J-S, Hoque MM, Nykiel G, Borries C, Morozova A, Barata T, Miloch WJ (2023) Ionosphere variability II: Advances in theory and modeling. Advances in Space Research In Press. https://doi.org/10.1016/j.asr.2023.07.056

Van den IJssel J, Forte B, Montenbruck O (2016) Impact of Swarm GPS receiver updates on POD performance. Earth Planet Sp 68:85. https://doi.org/10.1186/s40623-016-0459-4

Wang C, Guo W-L, Zhang Q-H, Zhao H-S, Cao L (2023) 3-D computerized ionospheric tomography with GPS, SAR, and Ionosonde. IEEE Trans Geosci Remote Sens 61:5210109. https://doi.org/10.1109/TGRS.2023.3285744

Wen D, Mei D, Chen H (2022) Three-step Tomographic Algorithm for Ionospheric Electron Density Reconstruction. IEEE Trans Geosci Remote Sens 60:5801408. https://doi.org/10.1109/TGRS.2021.3113667

Woodman RF (1970) Vertical drift velocities and east-west electric fields at the magnetic equator. J Geophys Res 75:6249–6259. https://doi.org/10.1029/JA075i031p06249

Yin P, Shi S, Ren D (2022) SBAS ionospheric grid delay estimation based on ionospheric tomography: a case study on September 7–9, 2017. GPS Solut 26:86. https://doi.org/10.1007/s10291-022-01259-7

Zhai C, Yao Y, Kong J (2021) Three-dimensional reconstruction of seismo-traveling ionospheric disturbances after March 11, 2011, Japan Tohoku earthquake. J Geod 95:77. https://doi.org/10.1007/s00190-021-01533-5

Zheng D, Yao Y, Nie W, Liao M, Liang J, Ao M (2021) Ordered subsets-constrained ART algorithm for Ionospheric Tomography by combining VTEC data. IEEE Trans Geosci Remote Sens 59:7051–7061. https://doi.org/10.1109/TGRS.2020.3029819

Zheng D, Yuan P, He C, Yao Y, Nie W, Lin D, Liao M, Xiong Z (2023) Virtual reference station technology for voxels without signal ray in ionospheric tomography based on machine learning. GPS Solut 27:166. https://doi.org/10.1007/s10291-023-01512-7

Zong Q-G, Reinisch BW, Song P, Wei Y, Galkin IA (2010) Dayside ionospheric response to the intense interplanetary shocks–solar wind discontinuities: observations from the digisonde global ionospheric radio observatory. J Geophys Res 115:A06304. https://doi.org/10.1029/2009JA014796

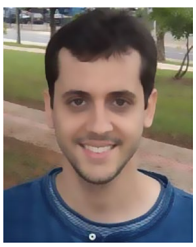

Fabricio S. Prol received the Ph.D. degree in cartographic sciences from the Sao Paulo State University, São Paulo, Brazil, with focus in geodetic remote sensing and geodetic positioning, in 2019. He worked as a Research Scientist in the German Aerospace Center (DLR) from 2019 until 2021. He has been working with the Finnish Geospatial Research Institute, Helsinki, Finland, since 2021. His research interests include ionospheric modeling, GNSS positioning, LEO-PNT navigation, and data assimilation.

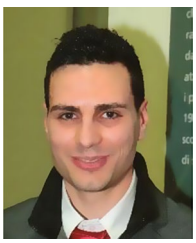

Alessio Pignalberi received the Master of Science degree in Physics from *Sapienza University of Rome* in 2014, and the Ph.D. degree in Geophysics from the *University of Bologna* in 2019 for his work on a three-dimensional regional assimilative model of the ionospheric electron density. Since 2019 he has been working with the *Istituto Nazionale di Geosifica e Vulcanologia* (INGV) in Rome, first as a post-doctoral fellow and since 2023 as a permanent researcher. He is conducting research in the field of Space Weather, radio-propagation in the ionosphere, ionosphere physics and modeling with particular focus on the improvement of ionospheric models like the *International Reference Ionosphere* (IRI) and *NeQuick*.

Artem Smirnov is a postdoctoral researcher at the Ludwig Maximilian University of Munich (LMU). He received the Ph.D. degree in Computational Physics working at the GFZ German Research Centre for Geosciences in Potsdam in 2023, and a joint master's degree in Geophysics from LMU and TUM in 2019. His research interests are focused on analyzing and modeling plasma populations in the ionosphere and magnetosphere of the Earth, particularly using machine learning techniques.

Michael Pezzopane received the M.Sc. degree in Physics from the "Sapienza" University of Rome, Italy, in 1997, and the Ph.D. degree in Geophysics from the University of Bologna, Italy, in 2005. Since 2001, he has been working with the Istituto Nazionale di Geofisica e Vulcanologia, in Rome, Italy. His main research interests include ionospheric physics and modeling, radio wave propagation in the ionosphere, Space Weather. He is a member of the International Reference Ionosphere Working Group.

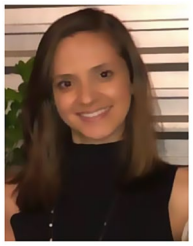

Ana Lucia Christovam is a postdoctoral researcher at the São Paulo State University (UNESP), Brazil. She received the Ph.D. in 2023 and a M.Sc. degree in Cartographic Sciences from São Paulo State University, Brazil, with focus in geodetic remote sensing and geodetic positioning, in 2019. Her research interests include ionospheric plasma bubbles, ionospheric modeling, and monitoring.

Kannan Selvan received his M.S degree in Communications and Systems Engineering from the University of Vaasa, Finland, and is currently pursuing a Ph.D. degree in Automation Technology. He is a Project Researcher in the Digital Economy Research Platform, interested in GNSS technologies, LEO-PNT, satellite-data analysis, machine learning and satellite communication.

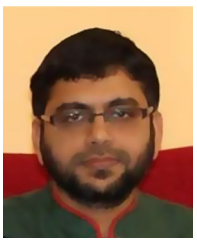

Mainul Hoque received his Bachelor in Electrical and Electronics Engineering in 2000 and was awarded a Ph.D. in 2009 from the University of Siegen, Germany. He has been working on ionosphere and plasmasphere modeling, propagation effects modeling including higher order terms at the German Aerospace Center (DLR) since 2004. Since 2019 he has been working as the Head of Department for Space Weather Observations, Institute for Solar-Terrestrial Physics, DLR. He was/is Involved and contributed in many national, international as well as ESA and EU projects related to ionosphere modelling and propagation delay corrections. He is the author/co-author of 3 patents and over 80 scientific papers in referred journals.

Sanna Kaasalainen received a Ph.D. in astronomy from the University of Helsinki, Helsinki, Finland, in 2003. She is currently a Professor and Head of the Department of Navigation and Positioning, FGI of the National Land Survey, Helsinki, Finland. Her research interests include resilient positioning, navigation and timing, situational awareness, and optical sensors. She also has research experience in LIDAR remote sensing, sensor development, and astronomy.